CHEMISTRY OF MATERIALS

Article

pubs.acs.org/cm

New 8-Layer Twinned Hexagonal Perovskite Microwave Dielectric Ceramics $Ba_8Ga_{4-x}Ta_{4+0.6x}O_{24}$

Jiang Cao,[†] Xiaojun Kuang,*[,†,‡] Mathieu Allix,[‡,§] Calum Dickinson,[‡] John B. Claridge,[‡] Matthew J. Rosseinsky,*[,‡] David M. Iddles,[⊥] and Qiang Su[†]

[†]MOE Key Laboratory of Bioinorganic and Synthetic Chemistry, State Key Laboratory of Optoelectronic Materials and Technologies, KLGHEI of Environment and Energy Chemistry, School of Chemistry and Chemical Engineering, Sun Yat-Sen University, Guangzhou 510275, P. R. China.

[‡]Department of Chemistry, The University of Liverpool, Liverpool, L69 7ZD, United Kingdom

[§]Conditions Extrêmes et Matériaux: Haute Température et Irradiation, CNRS UPR 3079, 1D Avenue de la Recherche Scientifique, 45071 Orléans Cedex 2, France and Université d'Orléans, Faculté des Sciences, Avenue du Parc Floral, 45067 Orléans Cedex 2, France

[⊥]Ceramic Division, Powerwave (U. K.) Ltd., Enterprise Drive, Station Road, Four Ashes, Wolverhampton, WV10 7DB, United Kingdom

Supporting Information

ABSTRACT: An 8-layer B-site deficient twinned hexagonal perovskite $Ba_8Ga_{4-x}Ta_{4+0.6x}O_{24}$ has been synthesized and its structure and microwave dielectric properties characterized. This hexagonal perovskite consists of eight close-packed BaO_3 layers stacked by a sequence of $(ccch)_2$, where c and h refer to cubic and hexagonal BaO_3 layers, respectively. The $Ba_8Ga_{4-x}Ta_{4+0.6x}O_{24}$ ceramic materials exhibit composition-independent dielectric permittivity $\varepsilon_r \approx 29$, improved Qf value with the B-site vacancy content increase, and tunable temperature coefficient of resonant frequency τ_f from negative to positive. An optimum microwave dielectric performance was achieved for $Ba_8Ga_{0.8}Ta_{5.92}O_{24}$: $Qf \approx 29\,000$ GHz and $\tau_f \approx 11$ ppm/°C. The factors controlling the microwave dielectric properties are discussed in comparison with 8-layer twinned analogues and related 10-layer twinned hexagonal perovskites based on their structural and property data.

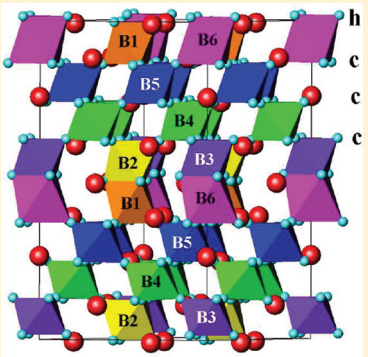

KEYWORDS: *hexagonal perovskite, microwave dielectric ceramic, site ordering, B-site deficiency*

INTRODUCTION

The development of component minimization for resonators and filters in microwave communication system requires high performance dielectric materials[1] (permittivity $20 < \varepsilon_r < 50$, quality factor $Q > 30\,000$ at 1 GHz, (Qf value is usually used as a figure of merit) and temperature coefficient of resonant frequency, $\tau_f \approx \pm 3$ ppm/°C). Among current commercial microwave dielectric materials, extensive attention has been focused on cubic perovskite materials such as B-site ordered complex perovskite $Ba_3B'B''_2O_9$ (B′ = Mg, Co, Zn; B″ = Nb, Ta)[1−3] and perovskite solid solution $CaTiO_3$−$NdAlO_3$[4] combining two end members with opposite signs on τ_f values. Recently hexagonal perovskites with mixed cubic (c) and hexagonal (h) staking of AO_3 layers received increasing interests on developing new microwave dielectrics because of their good microwave dielectric properties and the structural diversities with composition flexibility to accommodate diverse cations in A-sites and B-sites as well as vacancies in B-sites.[5−9] Hexagonal perovskite structures can be classified within two major kinds of twinned and shifted structures, depending on the occurrence of a single hexagonal layer (twinned) or two consecutive hexagonal layers (shifted) separating the cubic blocks.[10] It has been shown that fascinating microwave dielectric properties can be achieved on B-site deficient hexagonal perovskites such as the 5-layer shifted $BaLa_4Ti_4O_{15}$,[11] 8-layer twinned $Ba_8MTa_6O_{24}$ (M = Mg, Zn, Ni, Co),[12−15] and 8-layer shifted $Ba_8CoNb_6O_{24}$.[9] In the B-site deficiency hexagonal perovskites, corner-sharing octahedral (CSO) sites are fully occupied and B-site vacancies are confined on face-sharing octahedral (FSO) sites, reducing electrostatic repulsion between FSO cations at the short contact. The B-site vacancies either form a complete vacant octahedral layer between two hexagonal AO_3 layers in the shifted structure[5,9,10] or exhibit disordering or partial ordering in the twinned structure.[6,12]

Among the B-site deficient hexagonal perovskite microwave dielectric ceramics, $Ba_8MTa_6O_{24}$ materials are the most attractive as they exhibit $\varepsilon_r \approx 29$, high Qf values ~70 000−90 000 GHz, although the relatively high τ_f values were within ~30−45 ppm/°C.[12−15] The 8-layer twinned structure of

Received: August 31, 2011
Revised: October 10, 2011
Published: October 26, 2011

ACS Publications © 2011 American Chemical Society

$Ba_8MTa_6O_{24}$ consists of cubic and hexagonal BaO_3 layers stacked in a sequence of $(ccch)_2$ in space group $P6_3cm$, and exhibits partial cation and vacancy ordering in the FSO sites[12,16] leading to expanded cell parameters by $\sqrt{3}$ in the *ab* plane with respect to those in the simple 8-layer hexagonal perovskite cell. The B-cation and vacancy ordering in the FSO sites plays a key role on controlling the microwave dielectric loss.[6] Increase of the cubic layers in the 10-layer twinned hexagonal perovskites $Ba_{10}Mg_{0.25}Ta_{7.9}O_{30}$ and $Ba_{10}Co_{0.25}Ta_{7.9}O_{30}$ with enhanced vacancy content and disorder of cations and vacancies over the FSO sites led to larger microwave dielectric loss.[6] In this study, we report isolation of a new 8-layer twinned hexagonal perovskite $Ba_8Ga_{4-x}Ta_{4+0.6x}O_{24}$ with variable B-site vacancy content, and its microwave dielectric properties, cation and vacancy ordering, and microstructure of resonators.

EXPERIMENTAL SECTION

Synthesis. Polycrystalline samples of $Ba_8Ga_{4-x}Ta_{4+0.6x}O_{24}$ ($0 \leq x \leq 3.6$) for phase relationship investigation were synthesized from a mixed oxide route using $BaCO_3$ (Alfa-Asear, 99.997%+), Ga_2O_3 (Alfa-Aesar, 99.999%,) and Ta_2O_5 (Starck, 99%+) as starting materials. Stoichiometric amounts of $BaCO_3$, Ga_2O_3 and Ta_2O_5 in ~2 g batches were weighed and mixed in ethanol with an agate mortar and pestle. The dried mixtures were calcined at 1200 °C for 12hrs in alumina crucibles. These calcined powders were then ground, pressed into pellets and fired at 1450 °C for 24 h with heating and cooling rates of 5 °C/min.

The pellets of $Ba_8Ga_{4-x}Ta_{4+0.6x}O_{24}$ for microwave dielectric property measurement were made via the following processing. Stoichiometric amounts of $BaCO_3$, Ga_2O_3 and Ta_2O_5 in 20 g batches were weighed and ball-milled overnight with magnesia-stabilized zirconia beads using ethanol as mixing medium. After being dried at 80 °C to remove ethanol, the mixtures were calcined at 1200 °C for 12hrs, followed by ball-milling and drying again. The powders were uniaxially pressed into pellets using a 20 mm die, repressed again using a cold isostatic pressing facility and were fired at 1450 °C for 24 h with a heating rate of 5 °C/min and a cooling rate of 1 °C/min. The pellets reached >95% relative densities, which were calculated according to the weights and dimension of the pellets and their X-ray theoretical densities. The pellets were crashed into fine powder for X-ray and neutron diffraction structural analysis after microwave dielectric property characterization was performed.

Characterization. The X-ray diffraction (XRD) phase assemblage analysis in the samples were perform using a Panalytical X'pert Pro Multipurpose X-ray diffractometer (Co $K\alpha_1$ radiation λ = 1.78901 Å) and a D8 ADVANCE powder diffractometer (Cu $K\alpha$ radiation). XRD data of a quality suitable for Rietveld refinement was collected on the Panalytical X-ray diffractometer over the 10−120° 2θ range. Silicon was added as an internal standard during the laboratory XRD experiments to refine the cell parameters. Time-of-flight neutron diffraction (ND) data were collected on the high-resolution diffractometer (HRPD) at the ISIS facility (Rutherford Appleton Laboratory, UK). Rietveld analysis was performed with both XRD and ND data using Topas Academic software.[17] Bond valence sums (BVSs) were calculated by Brown and Altermatt's method.[18]

The electron diffraction (ED) study was carried out with a JEOL 2000FX transmission electron microscope (TEM). Energy dispersive X-ray spectroscopy (EDS) elementary analysis was performed on pellets of samples with a JXA-8800R electron probe microanalyzer. Graphite was coated on the samples to form a thin conducting layer prior to the EDS analysis, which was performed on fifteen regions for each sample.

Microwave dielectric properties were measured by a resonator reflection method.[19] τ_f was measured from −20 °C to 80 °C. AC impedance spectroscopy (IS) measurement was carried out by using a Solartron 1255B frequency response analyzer and a Solartron 1296 dielectric interface over $1-10^6$ Hz from 500 to 1000 °C. Pellets were coated with platinum paste and fired at 800 °C for 30 min to burn out the organic components to form electrodes prior to the IS measurement. The microstructure was examined using a Hitachi S4800 scanning electron microscopy.

RESULTS

$Ba_8Ga_{4-x}Ta_{4+0.6x}O_{24}$ Solid Solution. XRD data revealed the existence of a new phase in the sample with a nominal composition of Ba_2GaTaO_6 (x = 0 in $Ba_8Ga_{4-x}Ta_{4+0.6x}O_{24}$) as well as two known phases. The reflections of this new phase could be indexed with a hexagonal cell: $a \approx 10.048$ Å, $c \approx 18.975$ Å, which suggested an 8-layer hexagonal perovskite structure. The presence of $BaGa_2O_4$ and $Ba_4Ta_2O_9$ as minor phases was observed too.

Increasing the Ta^{5+} content along the $Ba_8Ga_{4-x}Ta_{4+0.6x}O_{24}$ line (Figure 1) between the nominal Ba_2GaTaO_6 (x = 0) and

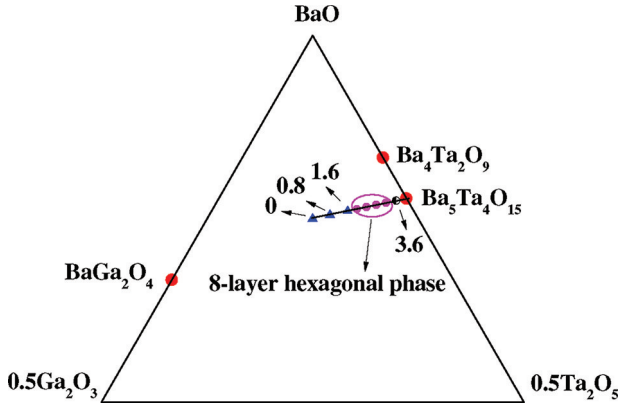

Figure 1. Representation of the selected compositions in the $BaO-Ga_2O_3-Ta_2O_5$ ternary diagram. The known phases ($BaGa_2O_4$, $Ba_4Ta_2O_9$, and $Ba_5Ta_4O_{15}$) are labeled using red filled circles. The $Ba_8Ga_{4-x}Ta_{4+0.6x}O_{24}$ (x = 2.0, 2.4, 2.8, 3.2) compositions isolated as single 8-layer hexagonal phase materials are plotted as pink filled-circles. The numbers denote the x values for $Ba_8Ga_{4-x}Ta_{4+0.6x}O_{24}$ samples appearing as mixtures.

$Ba_5Ta_4O_{15}$ (x = 4)) compositions led to a single 8-layer hexagonal phase within the x = 1.8 to 3.2 region. Further increase of the Ta^{5+} content in $Ba_8Ga_{4-x}Ta_{4+0.6x}O_{24}$ (x = 3.4, 3.6) led to mixture of the 8-layer hexagonal phase and the $Ba_5Ta_4O_{15}$ phase (a 5-layer shifted hexagonal perovskite structure). The XRD patterns of $Ba_8Ga_{4-x}Ta_{4+0.6x}O_{24}$ (x = 0.8−3.6) are shown in Figure 2.

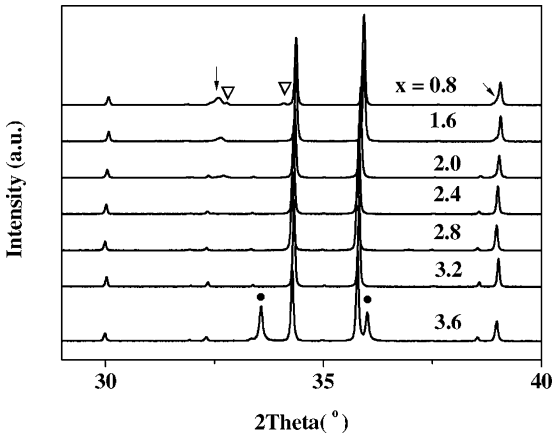

Figure 2. XRD patterns of $Ba_8Ga_{4-x}Ta_{4+0.6x}O_{24}$ (x = 0.8−3.6). The reflections from $BaGa_2O_4$, $Ba_4Ta_2O_9$, and $Ba_5Ta_4O_{15}$ are marked by ↓, ∇, and •, respectively.

Figure 3 shows the evolution of the refined cell parameters of the $Ba_8Ga_{4-x}Ta_{4+0.6x}O_{24}$ (x = 0.8−3.6) compositions, which suggests that the solid solution limit is situated between $1.8 \leq x \leq 3.4$. Within this solid solution limit, the cell parameters increase with x in the x = 1.8−2.8 region, followed by a drop for x = 3.2−3.4. EDS

dx.doi.org/10.1021/cm2025944 | Chem. Mater. 2011, 23, 5058−5067

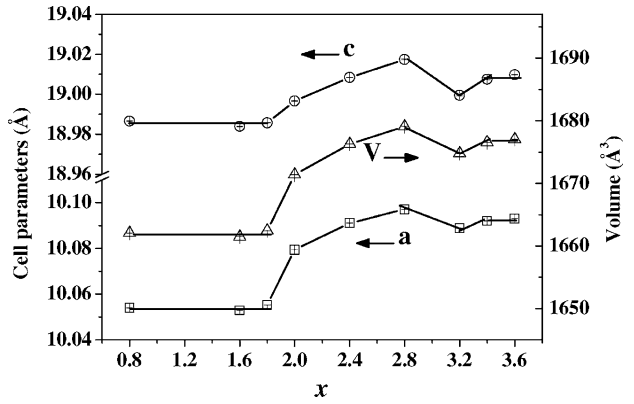

Figure 3. Cell parameters and volume of $Ba_8Ga_{4-x}Ta_{4+0.6x}O_{24}$ (x = 0.8−3.6).

elementary analysis performed on the solid solution as well as on $Ba_5Ta_4O_{15}$ and $Ba_3Ga_2O_9$ for comparison, which showed homogeneous cation ratios. The references gave a $Ba_5Ta_{3.57(5)}$ cationic composition for $Ba_5Ta_4O_{15}$ and $Ba_3Ga_{1.95(7)}$ for $Ba_3Ga_2O_9$. The cationic compositions were found to be $Ba_8Ga_{2.7(1)}Ta_{4.75(5)}$ for $Ba_8Ga_{2.2}Ta_{5.08}O_{24}$ (x = 1.8), $Ba_8Ga_{2.0(1)}Ta_{5.15(5)}$ for $Ba_8Ga_{1.6}Ta_{5.44}O_{24}$ (x = 2.4) and $Ba_8Ga_{0.9(1)}Ta_{5.61(5)}$ for $Ba_8Ga_{0.8}Ta_{5.92}O_{24}$ (x = 3.2), which essentially confirmed Ta and Ga contents over the solid solution limit. The large relative deviations for the Ga content measured in the $Ba_8Ga_{4-x}Ta_{4+0.6x}O_{24}$ samples is ascribed to the lower sensitivity of EDS to Ga regarding its lightness compared with the other elements.[6] Figure S1 in the Supporting Information shows the EDS spectra for selected $Ba_8Ga_{4-x}Ta_{4+0.6x}O_{24}$, compared with those for $Ba_5Ta_4O_{15}$ and $Ba_3Ga_2O_9$.

Structural Analysis. An ED study has been performed by tilting around the crystallographic axis. It confirmed the primitive hexagonal cell. The extra reflection conditions $000l$: $l = 2n$ and $h\bar{h}0l$: $l = 2n$ suggested the three following possible space groups: $P6_3cm$, $P\bar{6}c2$, and $P6_3/mcm$. A typical ED pattern recorded on the 8-layer hexagonal phase in x = 1.6 sample ($Ba_8Ga_{2.4}Ta_{4.96}O_{24}$) is shown in Figure 4.

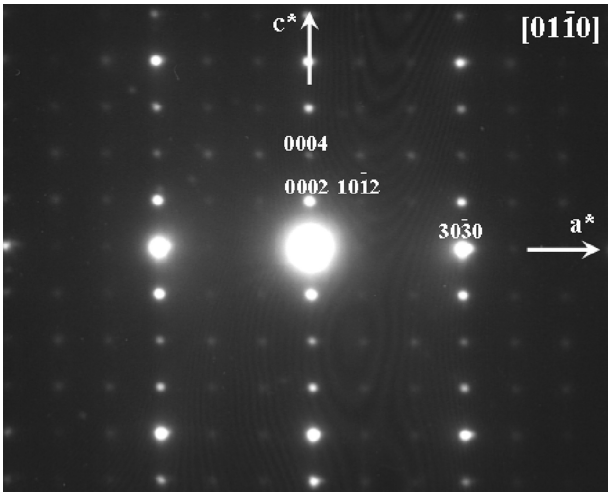

Figure 4. ED pattern projection along the [01$\bar{1}$0] direction for the 8-layer hexagonal perovskite phase in sample x = 1.6.

An 8-layer hexagonal perovskite structure with BaO_3 layers showing a $(ccch)_2$ stacking analogue to the $Ba_8ZnTa_6O_{24}$ structure was constructed in space groups $P6_3cm$ and $P6_3/mcm$. XRD Rietveld refinements performed on $Ba_8Ga_{4-x}Ta_{4+0.6x}O_{24}$ samples confirmed this 8-layer structure, which is incompatible with the $P\bar{6}c2$ space group, and suggested that the noncentric $P6_3cm$ is favored over the centric $P6_3/mcm$ ($R_{wp} \approx 9.96\%$, $R_B \approx 3.71\%$ for $P6_3cm$ versus $R_{wp} \approx 13.5\%$, $R_B \approx 4.73\%$ for $P6_3/mcm$ on the XRD data for sample x = 3.2), similar to $Ba_8ZnTa_6O_{24}$.

In the 8-layer hexagonal perovskite structure in noncentric $P6_3cm$ space group, there are six distinct crystallographic sites for B-cations (namely B1, B2, B3, B4, B5, and B6), as shown in Figure 5.

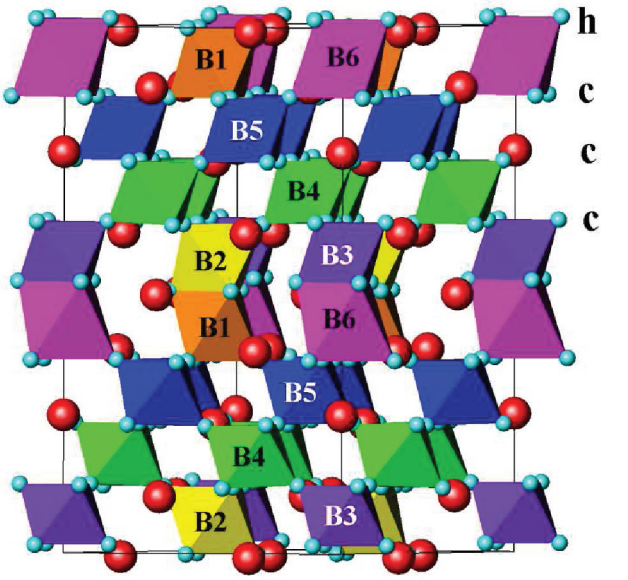

Figure 5. Eight-layer twinned perovskite structure of $Ba_8Ga_{0.8}Ta_{5.92}O_{24}$. The empty B6 octahedra (pink) are shown for illustrating the large thickness in contrast with the remaining octahedra.

Among these six B-sites, B4 and B5 are CSO sites and the remaining are FSO sites with two FSO dimers (B1−B2 and B3−B6). Rietveld structural analysis was performed on combined XRD and ND data for $Ba_8Ga_{4-x}Ta_{4+0.6x}O_{24}$. As the neutron scattering lengths of Ta and Ga are 6.91 fm and 7.288 fm,[20] respectively, the refinement of Ta^{5+} and Ga^{3+} occupancies mainly relied on XRD data. However, refinement of two cations and vacancies over the six B-sites remained tricky. A combined simulated annealing (SA) and Rietveld refinement approach, which has been proved reliable and successful on determining complex structures from powder diffraction data,[21−23] was then attempted to refine the cation and vacancy distribution over the B-sites. The refinement showed that the two CSO B4 and B5 sites are fully occupied (>80% Ta^{5+}) and that the B-site vacancies are distributed on the FSO sites only.

The refined cationic compositions for the x = 3.2 and 2.0 materials near the solid solution limit ($x \approx$ 1.8−3.4) revealed by EDS and XRD analysis are $Ba_8Ga_{0.52(9)}Ta_{5.94(8)}$ and $Ba_8Ga_{1.78(8)}Ta_{5.27(7)}$, respectively. The refined Ta contents agree well with the expected ones in the x = 3.2 and 2.0 materials within experimental errors. Both refined Ga contents for materials x = 3.2 and 2.0 show larger negative deviations from the expected ones in comparison with those for the refined Ta contents. This is ascribed to the lower sensitivity of XRD to Ga than to the heavy Ta atoms although the possibility of small amount of Ga volatilization cannot be completely excluded.

The refinement shows that in the x = 3.2 sample the B1−B2 dimer contains 0.19(5)□/0.72(2)Ta/0.09(3)Ga (□ denotes vacancy) on the B1 site and 0.47(5)□/0.32(2)Ta/0.21(3)Ga on

dx.doi.org/10.1021/cm2025944 | Chem. Mater. 2011, 23, 5058−5067

Table 1. Final Refined Structural Parameters for Sample $x = 3.2$ ($Ba_8Ga_{0.8}Ta_{5.92}O_{24}$)*

atom	site	x	y	z	occupancy	B_{iso}(Å^2)
Ba1	2*a*	0	0	0.2622(3)	1.0	1.7(2)
Ba2	4*b*	1/3	2/3	0.2434(3)	1.0	0.35(5)
Ba3	6*c*	0.6546(6)	0	0.6075(3)	1.0	1.50(8)
Ba4	6*c*	0.3126(4)	0	0.8837(3)	1.0	0.50(7)
Ba5	6*c*	0.3324(7)	0	0.4910(3)	1.0	0.34(3)
B1	4*b*	1/3	2/3	0.4353(4)	0.72(2)Ta/0.09(3)Ga	0.71(2)
B2	4*b*	1/3	2/3	0.0634(4)	0.32(2)Ta/0.42Ga[a]	0.71(2)
B3	2*a*	0	0	0.0577(4)	1.00(3)Ta	0.71(2)
B4	6*c*	0.3271(4)	0	0.6823(3)	1.00(2)Ta	0.71(2)
B5	6*c*	0.6570(4)	0	0.8072(3)	0.94(2)Ta/0.06(2)Ga	0.71(3)
O1	6*c*	0.5099(3)	0	0.2422(4)	1.0	0.6(1)
O2	6*c*	0.1897(5)	0.1897(5)	0.8679(4)	1.0	0.55(9)
O3	6*c*	0.1640(6)	0.1640(6)	0.5164(3)	1.0	1.19(6)
O4	12*d*	0.6676(7)	0.1760(4)	0.4970(3)	1.0	0.61(2)
O5	12*d*	0.3348(7)	0.1696(4)	0.2456(4)	1.0	0.74(6)
O6	12*d*	0.6715(6)	0.1607(6)	0.1247(4)	1.0	1.83(7)
O7	6*c*	0.1565(6)	0.1565(6)	0.1304(4)	1.0	0.56(9)
O8	12*d*	0.5057(5)	0.3449(5)	0.8640(4)	1.0	1.04(6)

*Space group $P6_3cm$, $Z = 3$, $a = 10.08630(2)$ Å, $c = 18.99469(5)$ Å, $V = 1673.504(8)$ Å^3. $R_{wp} \approx 3.56\%$, $R_B \approx 1.29\%$ on ND data; $R_{wp} \approx 10.1\%$, $R_B \approx 3.79$ on XRD data. The atomic displacement factors for *B*-cations have been constrained to identical values. [a]The 0.42 Ga on the B2 site contains the refined 0.21(3) and imposed 0.21 Ga.

Table 2. Bond Lengths and Bond Valence Sums (BVSs) for the $x = 3.2$ Sample ($Ba_8Ga_{0.8}Ta_{5.92}O_{24}$)

bond	bond length (Å)	bond	bond length (Å)	bond	bond length (Å)
Ba1−O2(× 3)	2.774(7)	Ba4−O2(× 2)	2.768(3)	B1−O4(× 3)	1.977(7)
Ba1−O5(× 6)	2.941(6)	Ba4−O4(× 2)	2.860(8)	B1−O8(× 3)	2.161(7)
Ba1−O7(× 3)	2.959(8)	Ba4−O3(× 1)	2.934(8)	$(BVS)_{Ta/Ga}$ at B1	4.14/2.48
$(BVS)_{Ba1}$	2.31	Ba4−O8(× 2)	3.016(5)	B2−O4(× 3)	2.031(8)
Ba2−O8(× 3)	2.843(6)	Ba4−O8(× 2)	3.043(4)	B2−O6(× 3)	2.116(8)
Ba2−O6(× 3)	2.864(7)	Ba4−O5(× 2)	3.055(9)	$(BVS)_{Ta/Ga}$ at B2	3.99/2.39
Ba2−O5(× 3)	2.900(6)	Ba4−O1(× 1)	3.228(9)	B1−B2(× 1)	2.43(1)
Ba2−O1(× 3)	2.9135(2)	$(BVS)_{Ba4}$	2.00	B3−O3(× 3)	1.831(7)
$(BVS)_{Ba2}$	2.41	Ba5−O2(× 1)	2.747(9)	B3−O7(× 3)	2.098(8)
Ba3−O3(× 1)	2.518(9)	Ba5−O4(× 2)	2.907(6)	$(BVS)_{Ta/Ga}$ at B3	5.67/3.40
Ba3−O4(× 2)	2.709(8)	Ba5−O4(× 2)	2.931(8)	B4−O6(× 2)	1.961(8)
Ba3−O6(× 2)	2.867(7)	Ba5−O3(× 2)	2.944(6)	B4−O7(× 1)	1.982(8)
Ba3−O6(× 2)	2.896(5)	Ba5−O8(× 2)	2.945(8)	B4−O1(× 1)	2.000(7)
Ba3−O1(× 1)	3.051(9)	Ba5−O6(× 2)	3.002(9)	B4−O5(× 2)	2.024(7)
Ba3−O7(× 2)	3.053(5)	Ba5−O7(× 1)	3.187(9)	$(BVS)_{Ta/Ga}$ at B4	4.95/2.96
Ba3−O5(× 2)	3.163(9)	$(BVS)_{Ba5}$	2.06	B5−O2(× 1)	1.929(7)
$(BVS)_{Ba3}$	2.53			B5−O8(× 2)	1.957(7)
$(BVS)_{O1}$[a]	2.00	$(BVS)_{O5}$[a]	1.90	B5−O1(× 1)	2.087(7)
$(BVS)_{O2}$[a]	2.06	$(BVS)_{O6}$[a]	1.98	B5−O5(× 2)	2.108(7)
$(BVS)_{O3}$[a]	2.32	$(BVS)_{O7}$[a]	1.96	$(BVS)_{Ta/Ga}$ at B5	4.63/2.77
$(BVS)_{O4}$[a]	1.97	$(BVS)_{O8}$[a]	1.94		

[a]The site occupancies of Ta/Ga at B sites were considered in the BVS calculation for oxygen atoms.

the B2 site and the B3−B6 dimer has a fully occupied B3 site (by Ta) and an empty B6 site. The CSO B4 site is occupied by Ta and B5 site contains 0.94(2)Ta/0.06(2)Ga. The Ga^{3+} cations are distributed over two FSO sites B1 and B2 and one CSO site B5. The B1 and B2 octahedral thicknesses in the FSO B1−B2 dimer are respectively ∼2.51 and ∼2.47 Å, which are in contrast with the large thickness (∼2.78 Å) for the empty B6 octahedron and the small thickness (∼2.20 Å) for the fully occupied B3 octahedron in the FSO B3−B6 dimer. This implies that the vacancy contents on the B1 and B2 sites are comparable. As Ta^{5+} and Ga^{3+} have close radii and the calculated BVSs for Ta and Ga on a same site show nearly identical relative deviation from the expected oxidation states, the BVSs of Ta(Ga) is not helping here on telling the site preference of Ta(Ga). The missing Ga content was then imposed on the B2 site only, leading to ∼26% vacancies on the B2 site, comparable to ∼19% vacancies on the B1 site, which coincide with the comparable BVSs of Ta(Ga) (4.17(2.50) on the B1 site versus 3.94(2.36) on the B2 site) in the B1−B2 dimer. This model gave $R_{wp} \approx 3.56\%$ on the ND data and ≈10.1% on the XRD data, compared to $R_{wp} \approx 3.41\%$ (ND) and ≈9.88% (XRD) from the refinement without composition constraint. The site occupancies of Ta(Ga) were involved in the calculation of BVSs for oxygen atoms, which vary from 1.90 to 2.32. Figure 5 shows the structure for the sample $x = 3.2$. Tables 1 and 2 list the final refined structural

dx.doi.org/10.1021/cm2025944|*Chem. Mater.* 2011, 23, 5058−5067

parameters and bond lengths for the x = 3.2 sample, respectively. The Rietveld refinement plots of XRD and ND data for the x = 3.2 sample are shown in Figure 6.

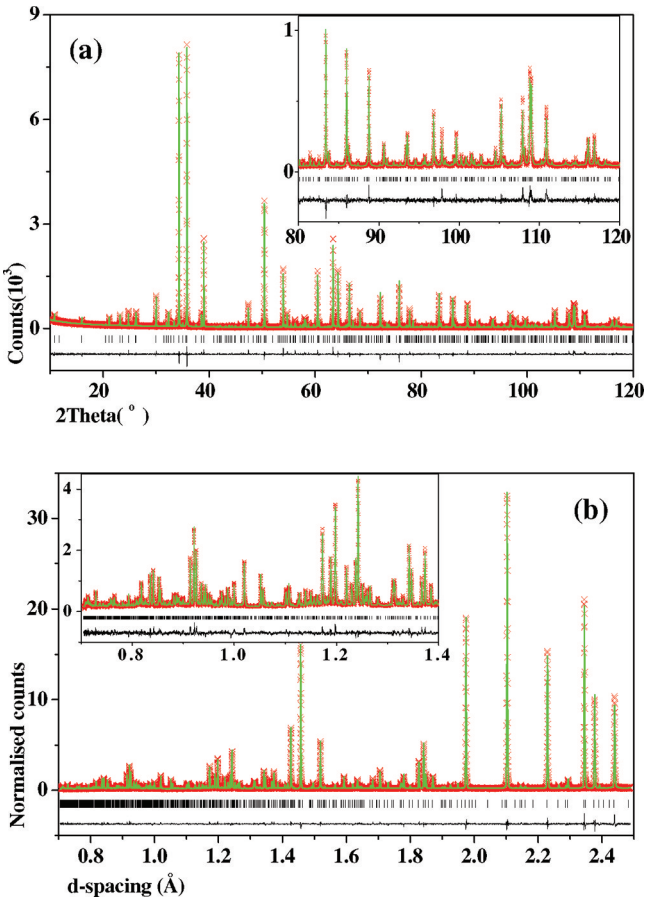

Figure 6. Rietveld refinement of (a) XRD and (b) ND data for the x = 3.2 sample ($Ba_8Ga_{0.8}Ta_{5.92}O_{24}$). The Bragg reflection positions are shown by tick marks. The insets in (a) and (b) enlarge the plots in the high 2θ range of 80–120° and low d-spacing range of 0.7–1.4 Å for XRD and ND data, respectively.

The x = 2.0 sample refinement shows that the B1–B2 dimer contains 0.06(4)□/0.52(2)Ta/0.42(2)Ga on the B1 site and 0.29(5)□/0.35(2)Ta/0.36(3)Ga on the B2 site. The B3–B6 dimer contains fully occupied B3 site by 0.80(3)Ta/0.20(3)Ga and 26(7)% occupied B6 site by 0.13(3)Ta/0.13(4)Ga. The partial occupation of the B6 site has been confirmed by difference Fourier map calculation. The Ga^{3+} cations are distributed over all six B-sites with refined Ga occupancies 0.13(2) and 0.14(2) on the CSO sites B4 and B5, respectively. Similar to the x = 3.2 sample case, the B1 and B2 sites show comparable octahedral thicknesses (~2.46 Å for the B1 site and ~2.43 Å for the B2 site) and BVSs of Ta(Ga) (4.41(2.64) for the B1 site and 4.29(2.57) for the B2 site), implying close vacancy contents on the B1 and B2 sites. Therefore, the missing Ga content was imposed on the B2 site only as the large B6 octahedron thickness (~2.74 Å) does not allow a high level of occupation on the B6 site (for sample x = 3.2, the B6 site is empty), leading to ~12% vacancies on the B2 site, compared to the ~6% vacancies on the B1 site. Tables 3 and 4 list the final refined structural parameters and bond lengths for the x = 2.0 sample, respectively. The BVSs for oxygen atoms for sample x = 2.0 vary from 1.86 to 2.26 (Table 4).

Microwave Dielectric Properties. The dependencies of ε_r, Qf, and τ_f on the composition for $Ba_8Ga_{4-x}Ta_{4+0.6x}O_{24}$ (x = 1.6–3.2) ceramics are shown in Figure 7. The $Ba_8Ga_{4-x}Ta_{4+0.6x}O_{24}$ pellets showed ≥95% relative densities and the porosity did not change with the composition significantly. The ε_r for $Ba_8Ga_{4-x}Ta_{4+0.6x}O_{24}$ ceramic is ~29 and almost independent of the composition except for the x = 1.6 pellet, which showed a smaller $\varepsilon_r \approx 26$, ascribed to the minor impurities detected by the XRD. The Qf value increases significantly with x in the 1.6–2.8 range and shows slight improvement when increasing x from 2.8 to 3.2. A maximum Qf value of ~29 000 GHz was achieved for x = 3.2. The τ_f value for $Ba_8Ga_{4-x}Ta_{4+0.6x}O_{24}$ ceramics is sensitive to the composition. The τ_f value increased significantly from negative (approximately −20 ppm/°C for the x = 1.6 pellet) to positive and reached a maximum value of ~27 ppm/°C for the x = 2.8 pellet then decreased down to ~11 ppm/°C for the x = 3.2 pellet.

Impedance Data. The impedance data measured on $Ba_8Ga_{4-x}Ta_{4+0.6x}O_{24}$ (x = 1.6–3.2) pellets comprise bulk and grain boundary responses. Figure 8a shows a typical complex impedance plot measured on sample x = 3.2 at 700 °C. The large semicircular arc corresponds to the bulk response with an associated capacitance of ~2.7 pF/cm, consistent with the permittivity measured at microwave frequency and the intercept of this semicircular arc in low frequency was estimated as bulk resistivity (Figure 8a); the tail in low frequency range is due to grain boundary response, which showed capacitance with a magnitude of ~1×10^{-9} F/cm. The Arrhenius plots for the bulk conductivities of $Ba_8Ga_{4-x}Ta_{4+0.6x}O_{24}$ pellets reveal a transition around 700 °C and activation energies show equally a transition from $E_a \approx$ 1.62–1.75 eV (temperature, T > 700 °C) to $E_a \approx$ 1.12–1.30 eV (T < 700 °C). Figure 8b shows a typical Arrhenius plot of the bulk conductivity corresponding to sample x = 3.2. Similar to the $Ba_8ZnTa_6O_{24}$ case, such an increase of the activation energy with temperature is ascribed to a change of the conduction mechanism from impurity ionization in the low temperature region (T < 700 °C) to excitation of electrons across the intrinsic gap (~3.2–3.5 eV) to conduction bands in the high temperature region (T > 700 °C).

Microstructure. The surface morphology of the $Ba_8Ga_{4-x}Ta_{4+0.6x}O_{24}$ ceramics has been examined by SEM and is shown in Figure 9. For the x = 1.6 pellet sample, the grains exhibit round shape with ~5–10 μm sizes. On the other hand, the x = 2.0 pellet sample shows that grain growth has started to exhibit anisotropy. Significant grain growth anisotropy can be observed for the x = 2.4, 2.8, and 3.2 compositions. For the x = 2.4 and 3.2 pellets, some abnormal large column-like grains with ~10–15 μm widths can observed, compared with the size of the x = 2.8 pellet (~2–6 μm).

DISCUSSION

B-Site Ordering. In the $Ba_8Ga_{4-x}Ta_{4+0.6x}O_{24}$ solid solution, the substitution of Ta^{5+} for Ga^{3+} creates vacancies on the B-sites according to the defect equation $5Ga_{Ga}^{\times} \leftrightarrow 3Ta_{Ga}^{\cdot\cdot} + 2V_{Ga}^{'''}$. The cell parameters of the $Ba_8Ga_{4-x}Ta_{4+0.6x}O_{24}$ solid solution exhibit nonlinear behavior within the overall solid solution limit (Figure 3). The increase of the cell parameters for x ranging from 1.8 to 2.8 is consistent with the greater Ta^{5+} ionic radius (0.64 Å for 6-coordinated Ta^{5+}) compared with Ga^{3+} (0.620 Å for 6-coordinated Ga^{3+}). The $Ba_8Ga_{4-x}Ta_{4+0.6x}O_{24}$ solid solution reached the largest cell parameters for x = 2.8. Beyond this point, the cell parameters dropped down to the level of the x = 2.4 composition, in spite of continuing substitution of Ta^{5+} for Ga^{3+} (from x = 3.2 to 3.4). As the EDS elementary analysis

dx.doi.org/10.1021/cm2025944 | Chem. Mater. 2011, 23, 5058–5067

Table 3. Final Refined Structural Parameters for the $x = 2.0$ Sample ($Ba_8Ga_{2.0}Ta_{5.12}O_{24}$)*

atom	site	x	y	z	occupancy	B_{iso}(Å^2)
Ba1	2*a*	0	0	0.2506(3)	1.0	0.55(5)
Ba2	4*b*	1/3	2/3	0.2346(4)	1.0	1.22(9)
Ba3	6*c*	0.6594(6)	0	0.6089(3)	1.0	0.55(4)
Ba4	6*c*	0.3168(4)	0	0.8843(3)	1.0	0.91(5)
Ba5	6*c*	0.3350(8)	0	0.4933(3)	1.0	0.57(2)
B1	4*b*	1/3	2/3	0.4209(2)	0.52(2)Ta/0.42(2)Ga	0.849(5)
B2	4*b*	1/3	2/3	0.0563(3)	0.35(2)Ta/0.53Ga[a]	0.849(5)
B3	2*a*	0	0	0.04877(7)	0.80(3)Ta/0.20(3)Ga	0.849(5)
B4	6*c*	0.3268(4)	0	0.6834(3)	0.87(2)Ta/0.13(2)Ga	0.849(5)
B5	6*c*	0.6649(5)	0	0.8063(2)	0.88(2)Ta/0.14(2)Ga	0.849(5)
B6	2*a*	0	0	0.4295(1)	0.13(3)Ta/0.13(4)Ga	0.849(5)
O1	6*c*	0.5059(5)	0	0.2435(4)	1.0	0.5(1)
O2	6*c*	0.1765(6)	0.1765(6)	0.8654(3)	1.0	0.83(9)
O3	6*c*	0.16778(5)	0.16778(5)	0.5101(2)	1.0	1.21(6)
O4	12*d*	0.6643(7)	0.1788(4)	0.4939(3)	1.0	1.25(3)
O5	12*d*	0.3325(7)	0.1663(7)	0.2460(3)	1.0	1.60(6)
O6	12*d*	0.6694(7)	0.1591(6)	0.1208(3)	1.0	1.55(6)
O7	6*c*	0.1668(6)	0.1668(6)	0.1276(3)	1.0	1.14(9)
O8	12*d*	0.5024(4)	0.3369(6)	0.8641(3)	1.0	1.14(6)

*Space group $P6_3cm$, $Z = 3$, $a = 10.07694(3)$Å, $c = 18.99142(9)$Å, $V = 1670.11(1)$Å^3. $R_{wp} \approx 3.46\%$, $R_B \approx 1.14\%$ on ND data; $R_{wp} \approx 9.50\%$, $R_B \approx 2.46$ on XRD data. The atomic displacement factors for B-cations have been constrained to identical values. [a]The 0.53Ga on the B2 site contains the refined 0.36(3) and imposed 0.17 Ga.

Table 4. Bond Lengths and Bond Valence Sums (BVSs) for the $x = 2.0$ Sample ($Ba_8Ga_{2.0}Ta_{5.12}O_{24}$)

bond	bond length (Å)	bond	bond length (Å)	bond	bond length (Å)
Ba1−O2(× 3)	2.814(7)	Ba4−O2(× 2)	2.794(4)	B1−O4(× 3)	1.991(6)
Ba1−O7(× 3)	2.877(7)	Ba4−O4(× 2)	2.821(7)	B1−O8(× 3)	2.076(6)
Ba1−O5(× 6)	2.903(6)	Ba4−O3(× 1)	2.822(6)	$(BVS)_{Ta/Ga}$ at B1	4.44/2.66
$(BVS)_{Ba1}$	2.45	Ba4−O8(× 2)	2.970(5)	B2−O4(× 3)	1.948(6)
Ba2−O6(× 3)	2.793(6)	Ba4−O8(× 2)	3.047(6)	B2−O6(× 3)	2.153(7)
Ba2−O1(× 3)	2.9146(6)	Ba4−O5(× 2)	3.076(7)	$(BVS)_{Ta/Ga}$ at B2	4.38/2.62
Ba2−O5(× 3)	2.924(6)	Ba4−O1(× 1)	3.226(8)	B1−B2(× 1)	2.571(7)
Ba2−O8(× 3)	2.975(5)	$(BVS)_{Ba4}$	2.10	B3−O3(× 3)	1.844(2)
$(BVS)_{Ba2}$	2.31	Ba5−O4(× 2)	2.877(9)	B3−O7(× 3)	2.251(6)
Ba3−O3(× 1)	2.560(6)	Ba5−O6(× 2)	2.892(7)	$(BVS)_{Ta/Ga}$ at B3	4.91/2.94
Ba3−O4(× 2)	2.816(7)	Ba5−O2(× 1)	2.907(9)	B4−O7(× 1)	1.9294(7)
Ba3−O6(× 2)	2.879(8)	Ba5−O4(× 2)	2.932(6)	B4−O6(× 2)	2.011(7)
Ba3−O6(× 2)	2.899(6)	Ba5−O3(× 2)	2.941(7)	B4−O5(× 2)	2.032(8)
Ba3−O7(× 2)	2.994(5)	Ba5−O8(× 2)	2.972(7)	B4−O1(× 1)	2.036(7)
Ba3−O1(× 1)	3.052(9)	Ba5−O7(× 1)	3.063(9)	$(BVS)_{Ta/Ga}$ at B4	4.75/2.84
Ba3−O5(× 2)	3.120(7)	$(BVS)_{Ba5}$	2.10	B5−O2(× 1)	1.953(8)
$(BVS)_{Ba3}$	2.36			B5−O8(× 2)	2.005(6)
$(BVS)_{O1}$[a]	1.86	$(BVS)_{O5}$[a]	1.98	B5−O5(× 2)	2.040(8)
$(BVS)_{O2}$[a]	1.91	$(BVS)_{O6}$[a]	1.94	B5−O1(× 1)	2.094(8)
$(BVS)_{O3}$[a]	2.26	$(BVS)_{O7}$[a]	1.92	$(BVS)_{Ta/Ga}$ at B5	4.58/2.74
$(BVS)_{O4}$[a]	1.98	$(BVS)_{O8}$[a]	1.99	B6−O2(× 3)	2.154(6)
				B6−O3(× 3)	2.261(3)
				$(BVS)_{Ta/Ga}$ at B6	2.72/1.63
				B6−B3(× 1)	2.266(3)

[a]The site occupancies of Ta/Ga at B sites were considered in the BVS calculation for oxygen atoms.

results clearly excluded the possibility of composition drifting to smaller Ta/Ga ratio in the $x = 3.2$ sample, the decrease in the cell parameters for $Ba_8Ga_{4-x}Ta_{4+0.6x}O_{24}$ close to the Ta^{5+}-rich solid solution limit (i.e., $x = 3.2-3.4$) suggests a competitive role between the B-site vacancies and the Ta^{5+} content on the cell parameters.

The 8-layer twinned hexagonal perovskite $Ba_8Ga_{4-x}Ta_{4+0.6x}O_{24}$ solid solution is only stable for a B-site vacancy content ranging from 9% to 17%. The mixture nature of the nominal Ba_2GaTaO_6 (i.e., $Ba_8Ga_4Ta_4O_{24}$) end member showing no B-site deficiency demonstrates that vacancies on B-sites stabilized the 8-layer twinned hexagonal phase. Higher B-site vacancies (20%) in the $Ba_5Ta_4O_{15}$ end member ends up to a 5-layer shifted hexagonal perovskite with a complete vacant octahedral layer between two consecutive hexagonal layers.[24] Similar to the $Ba_8ZnTa_6O_{24}$[6,12] and $Ba_8NiTa_6O_{24}$[16] cases, the B-site vacancies in $Ba_8Ga_{4-x}Ta_{4+0.6x}O_{24}$ are distributed over the FSO sites only. The introduction of B-site vacancies into FSO sites is favorable to

dx.doi.org/10.1021/cm2025944 | Chem. Mater. 2011, 23, 5058–5067

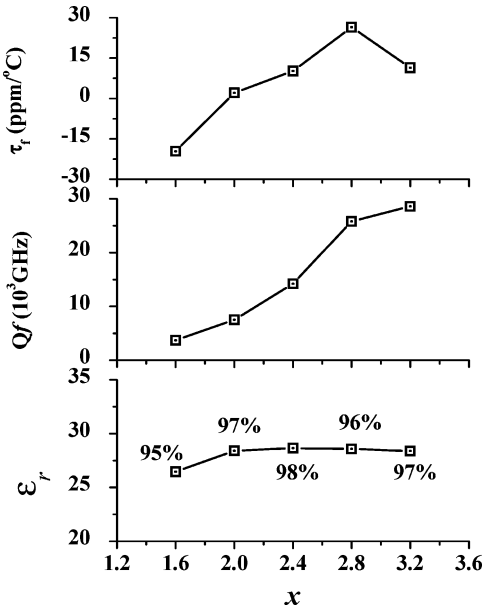

Figure 7. Microwave dielectric properties for $Ba_8Ga_{4-x}Ta_{4+0.6x}O_{24}$ (x = 1.6–3.2) ceramics. The numbers denote the relative densities of the pellets.

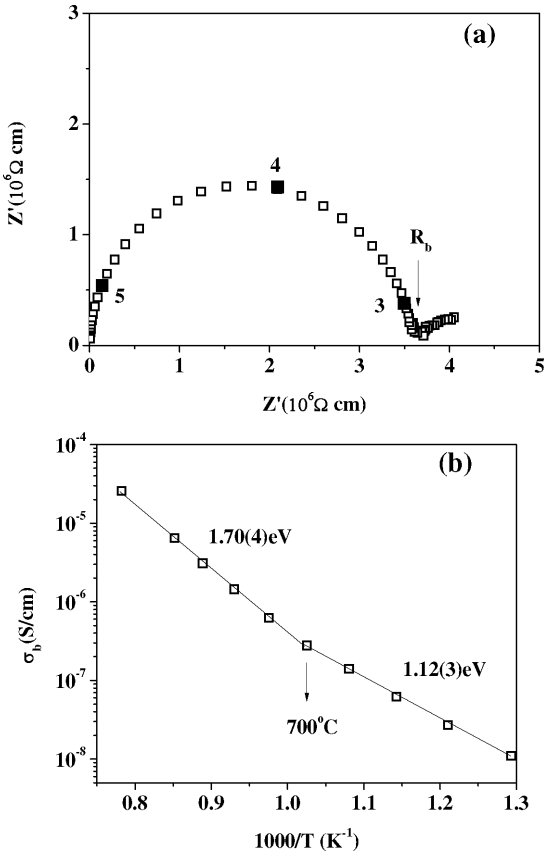

Figure 8. (a) Complex impedance plot recorded at 700 °C and (b) Arrhenius plot of the bulk conductivity for sample x = 3.2 ($Ba_8Ga_{0.8}Ta_{5.92}O_{24}$). The numbers denote the logarithm values of the selected frequencies marked by filled squares.

reducing the electrostatic repulsion between the FSO B-cations because of the short contact[25] thus stabilizing the 8-layer twinned hexagonal phase. The compounds containing Ga^{3+}–Ga^{3+} FSO d^{10}-cation dimers and Ta^{5+}–Ta^{5+} FSO d^0-cation dimers are rare. The Ga^{3+}–Ga^{3+} FSO distance close to 2.79 Å (in $BaGa_{12}O_{19}$[26]), is larger than those for the Cr^{3+}–Cr^{3+} FSO d^3-cation dimer (~2.52 Å in Ba_2CrNbO_6[27]) and the Mn^{4+}–Mn^{4+} FSO d^3-cation dimers (~2.53 Å in $La_4Ba_{2.6}Ca_{2.4}Mn_4O_{19}$[28]). The Ta^{5+}–Ta^{5+} FSO distance of ~2.88 Å (in $Ba_4Ta_2O_9$[29]), is larger those that for the common Ru^{5+}–Ru^{5+} FSO d^3-cation dimer (~2.57 Å in $Ba_3MgRu_2O_9$,[30] 2.69–2.67 Å in $Ba_6Na_2Ru_2M_2O_{17}$ (M = V and Mn)[31]) and Ti^{4+}–Ti^{4+} FSO d^0-cation dimer (~2.69 Å in $Ba_6Nd_2Ti_4O_{17}$,[32] ~2.72 Å in $Ba_6Y_2Ti_4O_{17}$,[32] ~2.67 Å in Hexagonal $BaTiO_3$[33]). These observed large distances of Ga^{3+}–Ga^{3+} and Ta^{5+}–Ta^{5+} in FSO dimers imply strong repulsions for Ga^{3+}–Ga^{3+} and Ta–-Ta^{5+} dimers. In $Ba_8Ga_{4-x}Ta_{4+0.6x}O_{24}$, the shorter B1–B2 distances ~2.43 Å (x = 3.2) and ~2.57 Å (x = 2.0) show that the vacancies at the FSO B-sites significantly reduced the repulsion between the FSO cations.

Similar to the cases of $Ba_8NiTa_6O_{24}$ and $Ba_8ZnTa_6O_{24}$, $Ba_8Ga_{4-x}Ta_{4+0.6x}O_{24}$ exhibits long-range partial cation and vacancy ordering among the FSO B-sites over the solid solution. Owing to the similar cationic sizes and less charge difference of Ga^{3+} and Ta^{5+} compared with Ni^{2+}(Zn^{2+}) and Ta^{5+}, $Ba_8Ga_{4-x}Ta_{4+0.6x}O_{24}$ exhibits enhanced B-cation distribution disorder, i.e. the Ga^{3+} cations are distributed over both the CSO and FSO B-sites, in contrast with that Ni^{2+} and Zn^{2+} cations are only confined in one FSO B-site in $Ba_8NiTa_6O_{24}$ and $Ba_8ZnTa_6O_{24}$, respectively. In the x = 2.0 sample, the Ga^{3+} cations show refined occupancies from 13% to 42% (in Table 3) over all the FSO and CSO B-sites with a preference on the FSO sites over the CSO sites. Whereas the lower Ga^{3+} content in the x = 3.2 sample led to Ga^{3+} occupation over two FSO sites and one CSO site with refined occupancies from 6% to 21% (in Table 1), showing reduced Ga^{3+}/Ta^{5+} distribution disorder with more substitution of Ta^{5+} for Ga^{3+}.

Microwave Dielectric Loss. The dielectric loss of ceramics includes intrinsic loss and extrinsic loss. The intrinsic loss refers to vibration anharmonicity of perfect lattice for the material and the extrinsic loss usually arises from the processing-sensitive factors including porosity, second phase, defects, site order etc. For the perovskite materials, microwave dielectric loss is sensitive to the B-site order driven by the differences of the sizes and charges between the B-cations. The 2:1 ordering of B-cations in complex perovskites leads to low microwave dielectric loss.[1,8,34,35] This has been ascribed to the minimization of the disordered charge distribution in the 2:1 ordered perovskite materials according to the Schlömann theory,[34] which predicted that the dielectric loss tan δ increases when the ions are distributed disorderedly in such a way that they break the periodic arrangement of charges in the crystal and that the increase of tan δ is negligible if the disordered charge distribution maintains the neutrality within a short-range with the order of lattice constant in the crystal. The cubic and hexagonal perovskites have common structural units but differ on the stacking because of the introduction of hexagonal layers into the cubic blocks in the hexagonal perovskite. The twinned hexagonal perovskite structure can be described as perovskite blocks assembled in a zigzag manner with each perovskite block sharing single h-BaO_3 layer with the adjacent blocks, forming two FSO layers. In some cases, the B-site vacancies are formed at the edge of the perovskite block to reduce the repulsion between the FSO B-cations at the short contact. The common structural units of cubic and hexagonal perovskite materials make them have similar factors on controlling the microwave dielectric properties, e.g., the relationship between temperature coefficient of resonate frequency and tolerance factors for the shifted hexagonal perovskites[5,36] is similar to that for the cubic

dx.doi.org/10.1021/cm2025944 | Chem. Mater. 2011, 23, 5058–5067

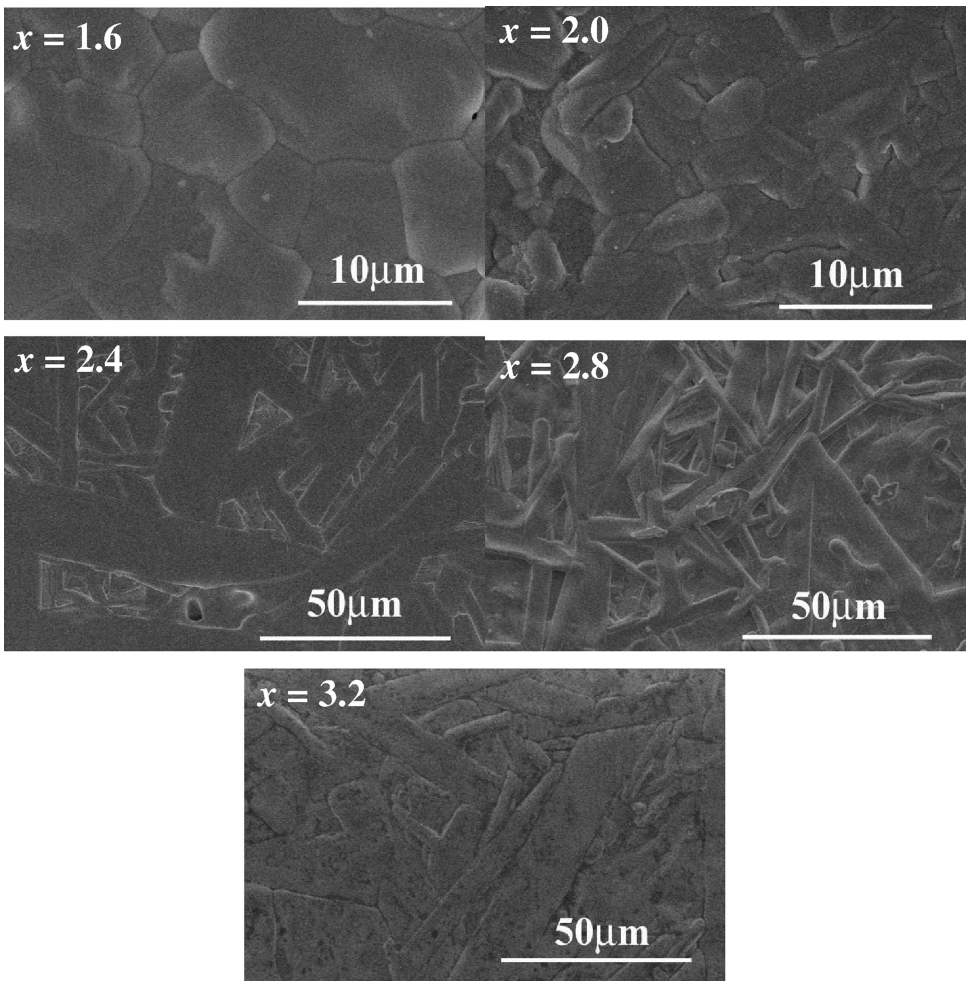

Figure 9. SEM images of surface morphology of the $Ba_8Ga_{4-x}Ta_{4+0.6x}O_{24}$ (x = 1.6–3.2) ceramics.

perovskite materials. The site ordering has been shown to have great influence on the microwave dielectric loss of the 8-layer and 10-layer twinned hexagonal perovskites according to Mallinson et al,[6] who proposed that the long-range partial ordering of B-cations and vacancies in the FSO layers offers the 8-layer twinned hexagonal perovskite $Ba_8ZnTa_6O_{24}$ lower microwave dielectric loss than the 10-layer twinned hexagonal perovskite $Ba_{10}Mg_{0.25}Ta_{7.9}O_{30}$ with enhanced disorder over the FSO layers. The $Ba_8Ga_{4-x}Ta_{4+0.6x}O_{24}$ solid solution shows lower Qf values than $Ba_8ZnTa_6O_{24}$; this could be ascribed to the more disordered Ga^{3+}/Ta^{5+} distribution over both the CSO and FSO B-sites in the perovskite blocks in the Ga-materials, which induced disordered charge distribution thus significantly increased the tan δ according to the Schlömann theory.[34]

The role of cation (charge) distribution on controlling the microwave dielectric loss of $Ba_8Ga_{4-x}Ta_{4+0.6x}O_{24}$ ceramics is more evident when the microwave dielectric loss for the $Ba_8Ga_{4-x}Ta_{4+0.6x}O_{24}$ ceramics is compared with some analogues[12−15,37,38] (in Table 5). The B-site ordering is driven by the difference between the sizes and charges of B-cations. It is possible to rank the B-site deficient 8-layer twinned hexagonal perovskites according to their B-site ordering in the following order: $Ba_8MTa_6O_{24}$ (M = Zn, Ni, Co, Mg) ($P6_3cm$) > $Ba_8Ga_{4-x}Ta_{4+0.6x}O_{24}$ ($P6_3cm$) > $Ba_8Ta(Nb)_{4-0.8x}Ti_{3-x}O_{24}$ ($P6_3/mcm$). Among the four FSO B-sites, the M^{2+} cation in $Ba_8MTa_6O_{24}$ is confined on the B2 site, which led to high Qf values (~69 000–91 000 GHz) for $Ba_8MTa_6O_{24}$ (M = Zn, Ni, Co, Mg) materials. On the contrary, the Ga^{3+} in $Ba_8Ga_{4-x}Ta_{4+0.6x}O_{24}$ or Ti^{4+} in $Ba_8Ta(Nb)_{4-0.8x}Ti_{3-x}O_{24}$ shows enhanced disordered distribution over both CSO and FSO B-sites, producing lower Qf values for $Ba_8Ga_{4-x}Ta_{4+0.6x}O_{24}$ ceramics (~10 000–29 000 GHz), $Ba_8Ta_{4-0.8x}Ti_{3-x}O_{24}$[38,39] and $Ba_8Nb_4Ti_3O_{24}$[37,38] (~10 000–23 000 GHz). More recently, the fully occupied B-site of the twinned 8-layer hexagonal perovskite $Ba_4LiTa_3O_{12}$ was shown to exhibit good microwave dielectric properties: $\varepsilon_r \approx 28$, $Qf \approx 104\,000$ GHz, and $\tau_f \approx 25$ ppm/°C,[7] comparable to those of $Ba_8ZnTa_6O_{24}$. In $Ba_4LiTa_3O_{12}$ ($P6_3/mmc$), the FSO dimers contain Li^+-Ta^{5+} distributed in a disordered manner[40,41] and the CSO sites are occupied by Ta^{5+} only. Presumably the charge distribution maintains the neutrality within $1/2c$ in the crystal by forming pure Li^+-Ta^{5+} FSO dimers in $Ba_4LiTa_3O_{12}$; this could offer high quality factor for $Ba_4LiTa_3O_{12}$ according to the Schlömann theory.[34]

In addition to the site/charge ordering controlling the microwave dielectric loss, the electrostatic cation repulsion in the FSO dimers is concerned here. In the $Ba_8Ga_{4-x}Ta_{4+0.6x}O_{24}$ case, besides the reduced charge disorder, the increased vacancies, which are favorable on minimizing the repulsion between the FSO B-cations, may contribute to reducing the microwave dielectric loss with the substitution of Ta^{5+} for Ga^{3+}. The $Ba_8Ta_{4-0.8x}Ti_{3-x}O_{24}$,[38,39] $Ba_8Nb_4Ti_3O_{24}$, and $Ba_8Ga_{4-x}Ta_{4+0.6x}O_{24}$ containing $Ta^{5+}(Nb^{5+})$ and tetravalent-(trivalent) cations in the FSO dimers exhibit low Qf values, whereas the $Ba_8MTa_6O_{24}$ (M = Zn, Ni, Co, Mg) and

dx.doi.org/10.1021/cm2025944 | Chem. Mater. 2011, 23, 5058–5067

Table 5. Microwave Dielectric Properties of Different 8-Layer and 10-Layer Twinned Hexagonal Perovskites

materials	space group	B-site vacancy content (%)	ε_r	Qf (GHz)	τ_f (ppm/°C)
$Ba_8Ga_{4-x}Ta_{4+0.6x}O_{24}$	$P6_3cm$	10−16	29	7500−28591	2−27
$Ba_8ZnTa_6O_{24}$[12,15]	$P6_3cm$	12.5	29	68224−78392	29.4−40
$Ba_8CoTa_6O_{24}$[15]	$P6_3cm$	12.5	29	69416	44
$Ba_8CuTa_6O_{24}$[15]	$P6_3cm$	12.5	29	8574	77
$Ba_8Mg_{0.75}Ni_{0.25}Ta_6O_{24}$[14]	$P6_3cm$	12.5	27	91327	26
$Ba_8NiTa_6O_{24}$[15]	$P6_3cm$	12.5	27	81758	32
$Ba_8Nb_4Ti_3O_{24}$[37,38]	$P6_3/mcm$[42]	12.5	38−49	12700−23500	115−125
$Ba_8Ta_{4-0.8x}Ti_{3-x}O_{24}$[38,39]	$P6_3/mcm$[43]	12.5−14.5	36−44	9720−23000	76
$Ba_8Li_2Nb_6O_{24}$[7]	$P6_3mmc$	0	37	57610	65
$Ba_8Li_2Nb_4Ta_2O_{24}$[7]	$P6_3mmc$	0	34	56040	43
$Ba_8Li_2Nb_2Ta_4O_{24}$[7]	$P6_3mmc$	0	30	37486	34
$Ba_8Li_2Ta_6O_{24}$[7]	$P6_3mmc$	0	28	103617	25
$Ba_{10}Co_{0.25}Ta_{7.9}O_{30}$[6]	$P6_3mc$	18.5	30	36693	29
$Ba_{10}Mg_{0.25}Ta_{7.9}O_{30}$[6]	$P6_3mc$	18.5	28	33585	30
$Ba_{10}Ta_{8-0.8x}Ti_xO_{30}$($x$ = 1.2−0.6)[38,39]	$P6_3/mmc$	17.6−18.8	34−35	25760−33200	52−64
$Ba_{10}Ta_{7.04}Ti_{0.45}Sn_{0.75}O_{30}$[38]	$P6_3mmc$	17.6	26	59100	30

$Ba_4LiTa_3O_{12}$ containing Ta^{5+} and divalent(monovalent) cations with less repulsion in the FSO dimers show high Qf values. This implies that the FSO cation repulsion is another factor affecting the microwave dielectric loss in addition to the disordered B-cation distribution discussed above.

In the BaO-TiO_2−Ta_2O_5 system,[42] the 8-layer twinned hexagonal perovskite phase $Ba_8Ta_{4-0.8x}Ti_{3-x}O_{24}$ (12.5−14.5% vacancy, $P6_3/mcm$) shows long-range FSO B-site ordering and the 10-layer twinned hexagonal perovskite phase $Ba_{10}Ta_{8-0.8x}Ti_xO_{30}$ (17.6−18.8% vacancy, $P6_3/mmc$) has disordered FSO B-sites. The 10-layer phase $Ba_{10}Ta_{8-0.8x}Ti_xO_{30}$ exhibits higher Qf values[38,39] than the 8-layer phase $Ba_8Ta_{4-0.8x}Ti_{3-x}O_{24}$ (Table 5). This can be explained by the reduced FSO B-cation repulsion coming from the increase of B-site vacancies in the 10-layer phase regardless of the enhanced B-site disorder in the 10-layer phase. On the other hand, in the BaO−MO−Ta_2O_5 (M = Mg, Zn, Ni) system, the disordered 10-layer twinned hexagonal perovskite $Ba_{10}Mg_{0.25}Ta_{7.9}O_{30}$[6] containing 18.5% B-site vacancies shows lower Qf value than the partially ordered 8-layer twinned hexagonal perovskite phases $Ba_8ZnTa_6O_{24}$[12] and $Ba_8Ni_{0.25}Mg_{0.75}TaO_{24}$[14] with less B-site vacancies (12.5%). This indicates that in the BaO−MO−Ta_2O_5 (M = Mg, Zn, Ni) system long-range B-site ordering plays a predominant role on controlling the microwave dielectric loss over the reduction of cation repulsion between FSO cations by B-site vacancies. Therefore, whether the B-site disordering or the FSO B-cation repulsion has predominate influence on the microwave dielectric loss for the hexagonal perovskites depends on the composition.

Temperature Coefficient of Resonant Frequency. The correlation between the tolerance factor and τ_f has been examined on the shifted B-site deficient hexagonal perovskites $A_nB_{n-1}O_{3n}$ (n = 5, 6),[5,36] which show a linkage of the tolerance factor with the sign of τ_f: a tolerance factor lower than 1 usually gives negative τ_f, and a tolerance greater than 1 usually gives positive τ_f. The tolerance factors of the twinned 8-layer and the 10-layer hexagonal perovskites vary within a narrow range of 1.03−1.05 and the τ_f values of the twinned 8-layer and 10-layer hexagonal perovskites are positive, as shown in Table 5. This agrees well with the observation made on the shifted $A_nB_{n-1}O_{3n}$ (n = 5, 6).[5,36] In $Ba_8Ga_{4-x}Ta_{4+0.6x}O_{24}$, the column-like anisotropic grains in the pellets x = 2.4, 2.8, and 3.2 are consistent with those in other analogues, e.g., $Ba_8Nb_4Ti_3O_{24}$[37] and $Ba_8ZnTa_6O_{24}$.[13] The samples x = 2.4 and 3.2 show similar microstructure of column grains with nonuniform widths (∼2−15 μm) and nearly identical τ_f values ∼10−11 ppm/°C. On the other hand, the x = 2.8 sample shows a more uniform column grains (∼2−6 μm on width) but a higher $\tau_f \approx$ 27 ppm/°C. The samples x = 1.6 and 2.0 contain more isotropic grains in the pellet instead. Sample x = 2.0 exhibits near zero τ_f (∼2 ppm/°C). While a negative τ_f was observed for x = 1.6 (approximately −20 ppm/°C). This could be due to the existence of minor impurities (∼3−5 wt %). It was shown that anisotropy of grain growth has great effect on the temperature coefficient of resonant frequency for some microwave dielectric ceramics such as B-cation deficient hexagonal perovskite type $BaLa_4Ti_4O_{15}$[44] and tungsten-bronze type $Ba_{6-3x}Sm_{8+2x}Ti_{18}O_{54}$.[45,46] The tunable τ_f observed in $Ba_8Ga_{4-x}Ta_{4+0.6x}O_{24}$ ceramics could be associated with the microstructure factors including the anisotropy of grain growth and grain sizes. Further investigation is required to confirm this hypothesis.

CONCLUSIONS

New $Ba_8Ga_{4-x}Ta_{4+0.6x}O_{24}$ 8-layer twinned hexagonal perovskite with variable B-site vacancy content was isolated and found to be isostructural with $Ba_8ZnTa_6O_{24}$. The microwave dielectric properties of dense pellets showed that the Qf increased with the B-site vacancy content and τ_f is tunable within the solid solution. An optimum microwave dielectric performance was achieved at $Ba_8Ga_{0.8}Ta_{5.92}O_{24}$: $\varepsilon_r \approx$ 29, $Qf \approx$ 29 000 GHz, and $\tau_f \approx$ 11 ppm/°C. The comparison of the $Ba_8Ga_{4-x}Ta_{4+0.6x}O_{24}$ structural and property data with other analogue 8-layer twinned hexagonal perovskites and some related 10-layer twinned hexagonal perovskites have allowed to elucidate the roles of site/charge disorder and the FSO B-cation repulsion on deteriorating the microwave dielectric loss. The tunable τ_f of $Ba_8Ga_{4-x}Ta_{4+0.6x}O_{24}$ demonstrates the plausibility of reducing the τ_f of the high-Q dielectrics $Ba_8MTa_6O_{24}$ (M = Mg, Zn, Ni, Co) analogues for application via controlling microstructure of ceramics.

ASSOCIATED CONTENT

Supporting Information

EDS elementary analysis data for $Ba_8Ga_{4-x}Ta_{4+0.6x}O_{24}$, $Ba_5Ta_4O_{15}$, and $Ba_3Ga_2O_9$; crystallographic information files in CIF format of the $Ba_8Ga_{0.8}Ta_{5.92}O_{24}$ (x = 3.2) and $Ba_8Ga_2Ta_{5.12}O_{24}$ (x = 2.0) compositions. This material is available free of charge via the Internet at http://pubs.acs.org/.

dx.doi.org/10.1021/cm2025944 | Chem. Mater. 2011, 23, 5058−5067

AUTHOR INFORMATION

Corresponding Author

*E-mail: kuangxj@mail.sysu.edu.cn (X.K.); m.j.rosseinsky@liverpool.ac.uk (M.J.R.).

ACKNOWLEDGMENTS

X.K., M.A., C.D., J.B.C., and M.J.R. thank EPSRC for Portfolio Partnership support (EPSRC/C511794). J.C., X.K., and Q.S. sincerely thank Sun Yat-Sen University and Guangdong Natural Science Foundation (S2011010001310) for financial support. We also thank Richard M. Ibberson (ISIS) for help on TOF ND data collection and Wenxia Zhao (Sun Yat-Sen University) for assistance on the EDS elementary analysis. Ivana R. Evans and John S. O. Evans (Durham University) are acknowledged for the permission to use the Macros for the Topas-Academic software for the structure refinements.

REFERENCES

(1) Reaney, I. M.; Iddles, D. *J. Am. Ceram. Soc.* **2006**, *89*, 2063−2072.
(2) Lufaso, M. W. *Chem. Mater.* **2004**, *16*, 2148−2156.
(3) Davies, P. K.; Borisevich, A.; Thirumal, M. *J. Eur. Ceram. Soc.* **2003**, *23*, 2461−2466.
(4) Nenasheva, E. A.; Mudroliubova, L. P.; Kartenko, N. F. *J. Eur. Ceram. Soc.* **2003**, *23*, 2443−2448.
(5) Kuang, X.; Allix, M. M. B.; Claridge, J. B.; Niu, H. J.; Rosseinsky, M. J.; Ibberson, R. M.; Iddles, D. M. *J. Mater. Chem.* **2006**, *16*, 1038−1045.
(6) Mallinson, P.; Claridge, J. B.; Iddles, D.; Price, T.; Ibberson, R. M.; Allix, M.; Rosseinsky, M. J. *Chem. Mater.* **2006**, *18*, 6227−6238.
(7) Fang, L.; Li, C. C.; Peng, X. Y.; Hu, C. Z.; Wu, B. L.; Zhou, H. F. *J. Am. Ceram. Soc.* **2010**, *93*, 1229−1231.
(8) Kuang, X.; Claridge, J. B.; Price, T.; Iddles, D. M.; Rosseinsky, M. J. *Inorg. Chem.* **2008**, *47*, 8444−8450.
(9) Mallinson, P. M.; Allix, M. M. B.; Claridge, J. B.; Ibberson, R. M.; Iddles, D. M.; Price, T.; Rosseinsky, M. J. *Angew. Chem., Int. Ed.* **2005**, *44*, 7733−7736.
(10) Trolliard, G.; Teneze, N.; Boullay, P.; Mercurio, D. *J. Solid State Chem.* **2004**, *177*, 1188−1196.
(11) Okawa, T.; Kiuchi, K.; Okabe, H.; Ohsato, H. *Jpn. J. Appl. Phys.* **2001**, *40*, 5779−5782.
(12) Moussa, S. M.; Claridge, J. B.; Rosseinsky, M. J.; Clarke, S.; Ibberson, R. M.; Price, T.; Iddles, D. M.; Sinclair, D. C. *Appl. Phys. Lett.* **2003**, *82*, 4537−4539.
(13) Thirumal, M.; Davies, P. K. *J. Am. Ceram. Soc.* **2005**, *88*, 2126−2128.
(14) Kawaguchi, S.; Ogawa, H.; Kan, A.; Ishihara, S. *J. Eur. Ceram. Soc.* **2006**, *26*, 2045−2049.
(15) Kan, A.; Ogawa, H.; Yokoi, A.; Ohsato, H. *Jpn. J. Appl. Phys.* **2006**, *45*, 7494−7498.
(16) Abakumov, A. M.; Tendeloo, G. V.; Scheglov, A. A.; Shpanchenko, R. V.; Antipov, E. V. *J. Solid State Chem.* **1996**, *125*, 102−107.
(17) Coelho, A. A. TOPAS Academic V4; Coelho Software: Brisbane, Australia, 2005.
(18) Brown, I. D.; Altermatt, D. *Acta Crystallogr., Sect. B* **1985**, *41*, 244.
(19) Kajfez, D.; Hwan, E. J. *IEEE Trans. Microwave Theory Techniques* **1984**, *32*, 666−670.
(20) Sears, V. F. *Neutron News* **1992**, *3*, 26−37.
(21) Li, M. R.; Kuang, X. J.; Chong, S. Y.; Xu, Z. L.; Thomas, C. I.; Niu, H. J.; Claridge, J. B.; Rosseinsky, M. J. *Angew. Chem., Int. Ed.* **2010**, *49*, 2362−2366.
(22) Evans, I. R.; Howard, J. A. K.; Evans, J. S. O. *J. Mater. Chem.* **2003**, *13*, 2098−2103.
(23) Kuang, X. J.; Li, Y. D.; Ling, C. D.; Withers, R. L.; Evans, I. R. *Chem. Mater.* **2010**, *22*, 4484−4494.
(24) Shannon, J.; Katz, L. *Acta Crystallogr., Sect. B* **1970**, *26*, 102−105.
(25) Keith, G. M.; Kirk, C. A.; K., S.; Alford, N. M.; Cussen, E. J.; Rosseinsky, M. J.; Sinclair, D. C. *Chem. Mater.* **2004**, *16*, 2007−2015.
(26) Wagner, T. R. *J. Solid State Chem.* **1998**, *136*, 120−124.
(27) Choy, J.-H.; Hong, S.-T.; Choi, K.-S. *J. Chem. Soc., Faraday Trans* **1996**, *92*, 1051−1059.
(28) Bie, L.; Wang, Y.; Lin, J.; Loong, C. K.; Richardson, J. J. W.; You, L.; Dong, C. *Chem. Mater.* **2003**, *15*, 516−522.
(29) Ling, C. D.; Avdeev, M.; Kharton, V. V.; Yaremchenko, A. A.; Macquart, R. B.; Hoelzel, M. *Chem. Mater.* **2010**, *22*, 532−540.
(30) Darriet, J.; Drillon, M.; Villeneuve, G.; Hagenmuller, P. *J. Solid State Chem.* **1976**, *19*, 213−220.
(31) Quarez, E.; Abraham, F.; Mentre, O. *J. Solid State Chem.* **2003**, *176*, 137−150.
(32) Kuang, X.; Jing, X.; Loong, C. K.; Lachowski, E. E.; Skakle, J. M. S.; West, A. R. *Chem. Mater.* **2002**, *14*, 4359−4363.
(33) Burbank, R. D.; Evans, H. T. *Acta Crystallogr.* **1948**, *1*, 330−336.
(34) Tamura, H. *J. Eur. Ceram. Soc.* **2006**, *26*, 1775−1780.
(35) Sagala, D. A.; Nambu, S. *J. Am. Ceram. Soc.* **1992**, *75*, 2573−2575.
(36) Santha, N. I.; Sebastian, M. T. *J. Am. Ceram. Soc.* **2007**, *90*, 496−501.
(37) Rawal, R.; Feteira, A.; Flores, A. A.; Hyatt, N. C.; West, A. R.; Sinclair, D. C.; Sarma, K.; Alford, N. M. *J. Am. Ceram. Soc.* **2006**, *89*, 336−339.
(38) Yokoi, A.; Ogawa, H.; Kan, A. *J. Eur. Ceram. Soc.* **2006**, *26*, 2069−2074.
(39) Baranov, A. N.; Oh, Y. J. *J. Eur. Ceram. Soc.* **2005**, *25*, 3451−3457.
(40) Jendrek, E. F.; Potoff, A. D.; Katz, L. *J. Solid State Chem.* **1974**, *9*, 375−379.
(41) Collins, B. M.; Jacobson, A. J.; Fender, B. E. F. *J. Solid State Chem.* **1974**, *10*, 29−35.
(42) Teneze, N.; Boullay, P.; Petricek, V.; Trolliard, G.; Mercurio, D. *Solid State Sci.* **2002**, *4*, 1129−1136.
(43) Shpanchenko, R. V.; Nistor, L.; Vantendeloo, G.; Vanlanduyt, J.; Amelinckx, S.; Abakumov, A. M.; Antipov, E. V.; Kovba, L. M. *J. Solid State Chem.* **1995**, *114*, 560−574.
(44) Fukami, Y.; Wada, K.; Kakimoto, K.; Ohsato, H. *J. Eur. Ceram. Soc.* **2006**, *26*, 2055−2058.
(45) Wada, K.; Kakimoto, K.; Ohsato, H. *J. Eur. Ceram. Soc.* **2003**, *23*, 2535−2539.
(46) Wada, K.; Kakimoto, K.; Ohsato, H. *Jpn. J. Appl. Phys.* **2003**, *42*, 6149−6153.

NOTE ADDED AFTER ASAP PUBLICATION

There was an error in the defect equation in the B-site Ordering section in the version published ASAP October 26, 2011; the corrected version published ASAP October 27, 2011.